Machine learning enabled microneedle-based colorimetric pH sensing patch for wound health monitoring and meat spoilage detection

Sachin Kadian^{1,*}, Pratima Kumari^{2,*}, Siba Sundar Sahoo³, Shubhangi Shukla¹, and Roger J.

Narayan^{1,3}

¹Joint Department of Biomedical Engineering, University of North Carolina and North Carolina State University, Raleigh, NC 27695, USA

²University of California San Francisco, San Francisco, CA 94143, USA
 ³Department of Materials Science and Engineering, North Carolina State University, Raleigh, NC 27695, USA

Corresponding author: Roger Narayan, Joint Department of Biomedical Engineering, University of North Carolina and North Carolina State University, Raleigh, NC 27695, USA, rjnaraya@ncsu.edu

First author email address: skadian@ncsu.edu

^{*}Authors have contributed equally to this work.

Abstract

Since pH can alter the biological functions, level of nutrients, wound healing process, and the behavior of chemicals, various healthcare and food industries are showing increased interest in manufacturing low-cost optical pH sensors for meat spoilage detection and wound health monitoring. To meet this demand, we have developed a simple and low-cost machine learningenabled microneedle-based colorimetric pH sensing patch that can be used for food quality and wound health monitoring applications. The 3D-printed ultrasharp open side channel microneedle array facilitated the autonomous fluid extraction and transportation via surface tension for colorimetric pH sensing. Further, to predict the exact pH value against the obtained color on the pH-test strip, a machine learning model was prepared using experimentally collected different color images obtained from a known pH solution. Furthermore, to make the device user-friendly for older individuals and color-blind individuals, a simple and smartphone-enabled web application was prepared using the developed machine learning model. The proof-of-concept study of the developed patch was demonstrated by determining the pH of real meat samples before and after spoilage and detecting pH in two different skin-mimicking in vitro models (phantom gel and parafilm tape) using a smartphone. The analytical results demonstrated that the developed machine learning-enabled microneedle-based colorimetric pH sensing patch has excellent potential for wound health and food safety applications.

Keywords

microneedle, colorimetric, biosensor, wound, machine learning monitoring, food monitoring

1. Introduction

Since an imbalance in the pH value can affect numerous processes, pH sensors play an important role in every domain, including chemical, biological, pharmaceutical, aquacultural, healthcare, agricultural, and food industries [1–7]. For instance, in pharmacy, it is essential to understand the influence of pH on the solubility and absorption of drugs [2,8–10]. Similarly, imbalanced pH can significantly affect the aquatic life and biological processes of the human body. Additionally, the pH value can also manipulate the behavior of chemicals, microbial activity, and biological functions; as such, the pH value can affect the wound healing process and level of nutrients in the food [11–13]. More specifically, wound healing is a complex process that is altered by several physicochemical and physiological parameters, including inflammatory mediators, pH, moisture, temperature, and nutrition factors [14-20]. Since the angiogenesis and collagen formation activities are highly dependent on the pH value of the wound-milieu, a small change in the pH level of the wound bed can significantly alter all biochemical reactions, which can slow down the healing processes of wounds and increase the possibility of bacterial colonization [21–24]. In normal conditions, due to the fatty acids and amino acids, the pH of healthy skin remains low and lies between 4-6. However, chronic wounds have a pH between 7 and 10 and thus are more susceptible to infection and formation of antibiotic-resistant biofilms, which upsurge the complications of the medical treatment [11,14,21,25]. Hence, observing the pH level of the wound can offer the real-time status of wounds and help decide the appropriate medical treatment. The existing clinical wound pH measurement procedures include conventional rigid glass pH probes, which can disrupt the healing tissue and cause unnecessary pain to the patient [11,26-29]. Therefore, developing intelligent and user-friendly pH sensors for wound health monitoring is highly desired.

Similarly, imbalanced pH can change microbial activity and result in food contamination, which can alter the organoleptic qualities of food and lead to spoilage [30–33]. Therefore, federal regulations demand that food suppliers preserve packed meat products in refrigerators below 4.4 °C and keep them fresh for the end users [34–37]. Although freezing is a good approach to decrease food spoilage, pathogenic bacterial species, including *L. monocytogenes* (responsible for 28% of foodborne disease-caused fatalities), can also grow at -0.4 °C temperature [38]. Additionally, it has been shown that commercial refrigerators can also demonstrate a temperature variation of ~10 °C

subjected to the light source and location, leading to spoilage. Therefore, to avoid foodborne diseases caused by eating contaminated meat, determining the freshness of refrigerated meat products before consumption carries significant importance [39–41]. The traditional meat freshness detection approaches involve microbial detection, organoleptic evaluation, and spectroscopic techniques, which require time-consuming sample preparation steps, are expensive, and are inaccurate [39]. Therefore, the development of new techniques that can be easily used by end users to monitor the freshness of individually packed meat products is of great significance. Among various meat freshness determining parameters, including temperature, odor, pH, biogenic amines, and color, pH has been recognized as a simple and more precise indicator of meat spoilage [39,42,43]. During the bacterial decomposition of meat items, the production of high pH value methylamines increases the overall pH of the meat surface and confirms the spoilage through a pH change. Further, it has been reported that the pH of fresh meat lies between 5.5 and 6.2; it is considered contaminated and unhealthy above a pH of 6.7 [39]. Therefore, due to the simple design, economical, accurate, and nondestructive approach for monitoring the freshness of meat products, colorimetric pH sensors on the packaging film have drawn significant consideration. These packing films utilize pH-sensitive dyes/compounds that change their color based on the pH value. Though these colorimetric pH sensing packaging films are economical and straightforward, they are also associated with a few limitations, such as poor contrast between the background and dye, challenges in interpreting color differences for older and color-blind consumers, delays in providing information, and the ability to detect only volatile substances in the packaging headspace. Hence, the development of intelligent colorimetric pH sensors that can address the abovementioned limitations is still required.

Recently, microneedle patches have emerged as an encouraging tool for healthcare and food quality monitoring applications by extracting the target analyte from interstitial fluid and food samples [44–46]. Therefore, in this study, we have developed a simple and low-cost machine learning-enabled microneedle-based colorimetric pH sensing patch (**Figure 1**) that can be used for both wound health and food quality monitoring applications. This pH sensing patch takes advantage of microneedle technology, 3D printing, paper-based pH sensing strips, a capillarity system, and machine learning models. The ultrasharp open side channel microneedle array equipped with a reservoir in their base facilitated the autonomous target fluid extraction and transportation via surface tension for colorimetric pH sensing. Further, a machine learning model

was prepared using experimentally collected different color images obtained from known pH value solutions to automatically predict the accurate pH value of the target analyte/solution. Furthermore, the developed model was deployed in order to create a web application for numerical representation of the detected pH level of the target analyte to provide the device with user-friendly features for older and color-blind individuals. The skin penetration, autonomous fluid extraction, and transportation capability of the developed microneedle patch via surface tension were investigated using two skin-mimicking *in vitro* models (phantom gel and parafilm tape) to demonstrate the wound health monitoring potential. Further, the proof-of-concept study of the developed patch was demonstrated by determining the pH of real meat samples before and after spoilage using a mobile phone. To the best of our knowledge, this report is the first illustration of a machine learning-enabled, microneedle-based, optical pH-sensing patch for meat spoilage and wound health monitoring applications.

2. Materials and methods

2.1 Materials

A glass fiber sample pad and cellulose absorbent pad were purchased from EMD Millipore (Burlington, MA, USA). The hydrophilic membrane and paper-based pH test strips were purchased from Sigma Aldrich, St. Louis, USA. Transparent plastic membrane and waterproof multipurpose tape were obtained from Amazon. All pH (2-12) reference standard buffer solutions were purchased from VWR International, LLC, Radnor, PA.

2.2 Microneedle design and fabrication

The high resolution (2μm~50μm) microneedle array (3 x 3) utilized in this study was prepared using an S130 additive manufacturing instrument (works on Projection Micro Stereolithography (PμSL) technology), which was provided by Boston Micro Fabrication (BMF), Maynard, MA, USA. The SolidWorks 2016 application (automation software) provided by Dassault Systems (Vélizy-Villacoublay, France) was used to design the microneedle structure having two conical shape needles with open side channels facing each other, a height of 1500 μm, a base diameter of 0.1 mm, and a diameter of 500 μm, culminating in a reservoir with a diameter of 0.4 mm. The microneedles were configured in 3 × 3 two-dimensional arrays (to ensure adequate analyte extraction) with a 1 mm spacing between two needles, which resulted in an overall miniatured

device footprint of 9×9 mm. The designed structure was sliced using BMF Slicer software, which is required for the 3D printing process. A yellow-colored photoreactive and biocompatible BIO resin (researched by the manufacturer via acute systemic toxicity, skin irritation, and in vitro cytotoxicity test), which was purchased from BMF, was utilized for microneedle array fabrication. The as-printed part was soaked in isopropyl alcohol to eliminate the remnants of unpolymerized resin from the reservoir and open side channels, followed by postprocessing under a (λ =405 nm) lamp (Formlabs Inc., MA, USA) for 10 min at 45°C.

2.3 Image data collection and Pre-processing

All machine learning-based color classification systems are required to be trained with a prior dataset to attain a remarkable classification performance, which is directly related to the features, quality, quantity, and diversity of a collected input dataset. Therefore, to create such a dataset of images representing different pH values, multiple smartphones (iPhone12, iPhone13, and iPhone13 Pro Max) and different light conditions, including white, yellow, and a combination of both, were used. Although more light conditions can be used to expand the input image dataset, the abovementioned sources were found to be sufficient for real-time applications. To ensure that the intensity of light and distance between the smartphone and pH sensing strip remains the same for all combinations, the images of pH sensing strips were collected under homogeneous illumination and at a fixed position of all objects. Since each smartphone has a unique camera, optics, and imaging software, the collected dataset was diverse even under the same illumination circumstances. To adjust the camera settings, such as exposure time, color temperature, and shutter speed, through the built-in imaging software, the automatic capturing mode was chosen over the manual capturing mode. A total of 1466 images were captured, which represents the input image dataset for pH values ranging from 2 to 12. Next, developing a classification model for the present study falls under the supervised machine learning task [47,48]. In order to perform this, the image dataset was suitably structured into different folders and labeled accordingly. Each folder was given a name that signified the category or label of the images contained within. Further, this dataset was divided into three subsets, including the training set, validation set, and test set, having 70%, 15%, and 15% of the total images, respectively, as demonstrated in the simplified flow chart of the developed classification model shown in Figure 2. The training set was used as the foundation for model learning, while the validation set was used for the hyperparameter tuning

and early stopping. The testing set was considered an unseen dataset, which served as the final evaluation benchmark for the classification model.

2.4 Machine Learning Model and User Interface

A Convolutional Neural Network (CNN) is a type of specialized deep learning model that is designed primarily for processing visual data and analyzing visual data, including videos and images, by automatically learning hierarchical features from visual data [49-52]. These models excel at capturing local patterns, edges, and textures in images, making them essential tools for a wide range of computer vision tasks, such as image classification, facial recognition, and object detection. Recently, CNN-based models have been widely used in various domains such as medical imaging, autonomous vehicles, robotics, and agriculture [53-55]. These processes involve the interpretation and understanding of images, relying on the information encoded in RGB (Red, Green, Blue) channels. An image is typically represented as having dimensions $X \times Y \times 3$, signifying X columns, Y rows, and three-color channels [53]. The basic architecture of a CNN model is shown in **Figure 3**. The core and first type of layers are convolutional layers, which play a pivotal role in feature extraction. It applies a set of learnable filters, which are also called kernels, with a specific size to the input images. The filter is moved across the image, performing elementwise multiplications and summing the results in order to create a feature map [56]. This operation helps the network capture different visual patterns, such as textures, edges, and shapes. Subsequently, the output from the convolution layer is fed into an activation function (typically ReLU) after each convolutional operation. The role of the activation function is to introduce the non-linearity in the model, which enables it to learn valuable complex patterns [57,58]. Further, convolutional layers are followed by pooling layers, which downsample the spatial dimensions of the feature maps, which reduce the computational complexity and the number of parameters in the network. These layers can employ various pooling operations, such as average pooling and max pooling. For example, max pooling takes the maximum value in a small window and retains it; average pooling takes the average of the window, which helps in retaining the most important features while reducing the spatial resolution. After several convolutional and pooling layers, the final layer in this network consists of one or more fully connected layers [59-61]. The fully connected layers flatten the feature maps into a 1D vector and connect each neuron to every neuron in the previous and subsequent layers. In this layer, an activation function, generally logistic or softmax, is applied to calculate probabilities. Higher probabilities indicate the presence of the

desired features in the image, thereby signifying a successful image classification process [62,63]. So far, several types of CNN models have been developed that vary according to the architecture and complexity of the convolutional layers, followed by pooling layers. These models include GoogLeNet (Inception), LeNet, AlexNet, VGGNet, and ResNet, which are trained on the ImageNet dataset, which includes 1.4 million images that belong to 1000 classes [64]. Therefore, in this work, we have used the VGGNet-based VGG16 architecture proposed by Karen Simonyan and Andrew Zisserman to build a classification model. VGG16 is used because of its simplicity and high performance, as it showed a significant advancement in the field of computer vision [65,66]. The architecture of VGG16 is deep; it is comprised of 16 weight layers, having 13 convolutional layers as well as 3 fully connected layers. In this approach, every convolutional layer is followed by a max-pooling layer for downsampling and reducing the spatial dimensions of the feature maps. VGG16 utilizes a large number of learnable filters in its convolutional layers that enable the model to capture a wide range of image features. In the present work, the last few layers of the VGG16 are trained according to our training dataset, and pre-trained weights for inner layers are kept frozen. A validation dataset is utilized to fine-tune hyperparameters; finally, the model is evaluated with the test dataset.

Further, in order to provide a better experience of using the developed model, the deep learning-based classification model is deployed as a custom-designed web application. The web application takes the image as the input and predicts the pH value for the given image. The web integration of the proposed classification model provides real-time utilization, accessibility, and user-friendliness to classify the given images based on their pH values. In order to develop the web application, initially, the model and its weights are saved, which is further integrated using Flask, Hyper Text Markup Language (HTML), and Cascading Style Sheets (CSS). For example, Flask is the most utilized open-source lightweight web framework that is built in Python, which helps in deploying web applications. Similarly, HTML and CSS provide the service to create an interface for taking input from the user. Flask takes the input value via application programming interface (API) calls, computes the predicted pH value using the classification model, and provides the output to the user.

2.5 Performance evaluation metrics

To assess the effectiveness of a machine learning model, the performance evaluation is a necessary step. In the present work, the overall performance of the developed classification model was measured using different evaluation metrics, including True Negatives (TN), True Positives (TP), False Negatives (FN), False Positives (FP), precision, accuracy, recall, and F1-score.

True Positives (TP):

True positives are instances that describe the situation in which the model correctly predicted the positive class, and the actual ground truth is also positive.

True Negatives (TN):

True negatives are instances that describe the situation in which the model correctly predicted the negative class, and the actual ground truth is also negative.

False Positives (FP):

False Positives are instances that describe the situation in which the model incorrectly predicted the positive class, but the actual ground truth is negative. FP are also known as Type I errors; false positives represent instances where the model wrongly identified something as positive when it is not.

False Negatives (FN):

False Negatives are instances that describe the situation in which the model incorrectly predicted the negative class, but the actual ground truth is positive. FN are also known as Type II errors; false negatives represent instances where the model fails to identify something as positive when it is.

Accuracy:

The accuracy measures the number of successfully predicted instances from the model. The accuracy can be determined as follows:

$$Accuracy = \frac{TP + TN}{TP + TN + FP + FN}$$

Precision:

Precision is calculated as the ratio of accurately predicted positive outcomes to all positive outcomes predicted by the model.

$$Precision = \frac{TP}{TP + FP}$$

Recall:

Recall is calculated as the ratio of accurately predicted positive outcomes to all actual positive items.

$$Recall = \frac{TP}{TP + FN}$$

F1-Score:

The F1-score value represents the harmonic mean of precision and recall. This value balances precision and recall; it is determined as follows:

$$F1 - Score = \frac{2 \times (Precision \times Recall)}{(Precision + Recall)}$$

2.6 Physical and mechanical characterization

The structural and morphological characterization of 3D-printed microneedles was performed with a Hitachi SU3900 (Tokyo, Japan) Scanning Electron Microscope (SEM) with an accelerating voltage range from 0.3 to 30 kV.

2.7 Fluid extraction and pH sensing through skin-mimicking models

The fluid extraction capability and wound health monitoring potential of the microneedle-based colorimetric pH sensing patch were examined by detecting the pH while penetrating two skin-mimicking models, namely a parafilm tape and a phantom gel. For this, a customized experimental setup was prepared. First, an 8 mm diameter hole was created in the cap of a small plastic box and placed in a small Petri dish. This Petri dish was then filled with different pH (2, 6, and 11) solutions while confirming no runoff. Further, the manually created circular hole was covered with parafilm tape and phantom gel to create two different experimental setups. Next, the microneedle-based colorimetric pH sensing patch was gently pushed so that the microneedle tips could penetrate the skin-mimicking models (parafilm layer and phantom gel) and make contact with the solution. The

macroscopic images and videos of the fluid extraction and pH sensing experiments were obtained through an iPhone 13 device (Cupertino, CA, USA). Further, to avoid any unwanted temperature-related interference in the analytical performance of the pH sensing probe, all the experiments were performed in a computer-controlled room temperature environment. For control experiments, a standard pH probe (PH700 Benchtop pH Meter Kit, Apera Instruments, LLC) was used to measure the actual pH of the particular samples; these results were compared with those of the pH sensing strips.

2.8 pH sensing of the real meat sample

To investigate the real-time application of the developed microneedle-based colorimetric pH sensing patch for food quality monitoring, the freshness of real meat samples was determined before and after spoilage. Fresh meat samples were purchased from the local supermarket and stored in appropriate freezing conditions before experiments. To prepare the spoiled meat sample, two different samples were exposed to pH 3 and pH 9 solution and kept outside the refrigerator but in a cold environment for 4 days. Next, to perform the experiments, the as-developed three different microneedle-based colorimetric pH sensing patches were placed on three different samples (fresh, exposed with pH 3 and pH 9 solution) and gently pressed so that the microneedle tips start extracting the fluid. Once the fluid extraction is completed, a smartphone is used to capture the image of the patch, which is uploaded to the developed web application for analysis and results. Furthermore, to prevent temperature-related interference in the analytical performance of the colorimetric pH sensing patch, all the experiments were performed in a room-temperature environment.

3. Results and Discussion

3.1 Fabrication and operation of microneedle-based colorimetric pH sensing patch

The schematic diagram and view of the fabrication process of the microneedle-based colorimetric pH sensing patch are shown in **Figure 4a**. The device comprises a waterproof multipurpose tape, a 3D-printed microneedle array, a hydrophilic membrane, a sample pad, paper-based pH sensing strips, an absorbent pad, and a transparent plastic membrane. Since the cavity of traditional hollow microneedles can be choked during analyte sampling, the microneedle array employed in the present device was engineered with open side channels, culminating in a reservoir constructed into

the base of microneedles [67,68]. To ensure the simple and uninterrupted extraction of the analyte, the reservoir was created between two microneedles with their open side channels facing each other, which resulted in an array of 18 needles with nine reservoirs. Such a model allows desirable analytes to be collected in the reservoir through the capillary effect posed by the open side channels. The 3D-printed microneedle array was attached to the adhesive tape at a designated cutout (Figure 4b (ii)) to prevent any unwanted leakage from the bottom side, as shown in Figure **4b** (ii). To ensure the autonomous and efficient extraction of the analyte, a hydrophilic membrane Figure 4b (iii) was in a sandwich arrangement between the microneedle array reservoir and lateral flow test strip (involving a cellulose sample pad, paper-based pH sensing strip, and absorbent pad) as shown in Figure 4b (iv). Further, to avoid any undesirable external moisture interference on the paper-based pH sensing strip through the result window, the entire lateral flow test strip was covered with a transparent plastic membrane (Figure 4b (v)) before sandwiching all components between two layers of waterproof tape. The white color tape was used to readily differentiate and quantify the obtained color of the test strip through imaging instruments and processing software. Figure 4c demonstrates the realistic image of the top and bottom view of the fully assembled pH sensing patch. Upon employing the developed pH sensing patch to the test surface (i.e., wound bed or meat sample) and gently pressing it, the microneedle array accesses the inner layers containing the analyte fluid and extracts via surface tension. The hydrophilic membrane helps autonomously transport the collected sample from the reservoir to the paper-based pH sensing strip via a glass fiber sample pad. As the collected sample travels toward the absorbent pad, the paperbased pH sensing strip starts reflecting the color corresponding to the pH of the sample. Afterward, the photo of the result window reflecting the change in color was captured and cropped using a smartphone. Finally, the cropped image was used for further analysis and determination of the pH value of the sample through a machine learning classifier to make the device user-friendly for older and color-blind individuals.

3.2 Characterization of microneedle array

Before utilizing the 3D-printed microneedle array for the development of the pH sensing patch, structural, morphological, and mechanical characterization of the microneedle array was performed. The micrometer-scale attributes of channels were confirmed through SEM images of the 3D-printed microneedle array, as shown in **Figure 5**. **Figure 5**b reveals the topographic and

tip sharpness characteristics of the microneedle array. It can also be noted from **Figure 5b** that the open side channels continued from the top of the needle to the reservoir. Further, the mechanical strength of the BIOresin material was previously determined through the nanoindentation method [69]. The hardness value and Young's modulus value of the material were previously shown to be 302.19 ± 10.44 MPa and 3.29 ± 0.12 GPa (mean \pm standard deviation), respectively. The Young's modulus value of microneedle material is higher than the minimum value (1 GPa) needed to puncture the human skin (Park et al., 2005). The 3D-printed microneedle array can be used for the fabrication of pH-sensing patches for multipurpose applications.

3.3 Fluid extraction and pH sensing through skin mimicking models for wound health monitoring

The autonomous fluid extraction capability of the microneedle array is also an important factor for the fabrication of a lateral flow test device. Therefore, two skin-mimicking models (parafilm tape and phantom gel) were used to investigate the capillary-based sample collection and real-time wound pH sensing potential of the developed pH sensing patch. Figures 6a and 6b show the customized fluid extraction experimental setup in which the circular hole was covered with parafilm tape, as discussed in Section 2. Next, the three different pH-sensing patches were applied to the skin-mimicking model, having three different pH solutions (2, 6, and 11). Upon gently pressing the patch, the sensing patch started extracting the sample via open side channels due to the surface tension and capillary action. The hydrophilic membrane facilitated the transportation of collected samples from the reservoir to the paper-based pH sensing strip via the glass fiber sample pad, leading to the color change of the test strip corresponding to the pH of the solution, as shown in Figures 6d, 6e, and 6f. Figure 6c demonstrates the optical image of pores created by the microneedle array on the parafilm tape after experiments, confirming that the microneedle array will cause minimal pain and no damage to the surrounding tissue when penetrated into the skin. Similarly, to confirm the real-time wound pH sensing functionality of the approach, the same experiment was repeated on another skin-mimicking model (phantom gel). Instead of parafilm tape, freshly prepared phantom gel was placed on the circular hole (Figures 7a and 7b). Next, the pH sensing patches were applied with phantom gel having access to three different pH (2, 6, and 11) solutions. Upon a gentle push, the sensing patch started extracting the sample from the phantom gel through capillary action and transported it to the paper-based pH sensing strip, resulting in the

change in color of the test strip, as shown in **Figures 7d**, **7e**, **and 7f**. **Figure 7c** reveals the optical image of phantom gel attached to the microneedle array after experiments, demonstrating the skin penetration capability of the microneedle array. In addition to the optical image of the pH sensing experiments shown in **Figures 6 and 7**, two short videos (Supplementary Video 1 and Video 2) of the entire fluid extraction and pH sensing process were also recorded and incorporated in the supplementary file. These *in vitro* results indicate that the developed pH sensing patch can easily extract the interstitial fluid by penetrating the skin-mimicking models, and can thus be used as a smart colorimetric sensor for wound health monitoring applications.

3.4 pH detection performance of machine learning model

Since the traditional estimation of pH through the color change of pH paper is associated with a high variance in pH value, which leads to the wrong assessment of pH using the naked eye, in this study, we have proposed a deep learning-based classification model for the detection of the pH value. The proposed model was prepared using pre-trained VGG16 architecture, in which the relu activation function was used in the inner layers, while softmax function was used in the outer layer. To fine-tune the model categorically, cross-entropy is used as the loss function. Next, the optimized values of other training parameters were as follows: batch size=32, learning rate=0.001, and maximum epoch =100. Further, the deep learning-based classification model was developed using the Python-based open source keras library; this study was performed using a workstation with Intel core i5-3470 3.20 GHz CPU, 32.0 GB RAM, and Nvidia GeForce GTX 1060.

Further, to investigate the prediction performance of the developed model, the trained and validated model was tested on unseen images to predict the pH class they belong to. The classification report of the developed model, which provides an evaluation of the performance of the model in terms of precision, recall, and f1 score for each pH class, is summarized in **Table 1.** It can be observed from the table that the overall accuracy of the model across all classes was found to be 0.98, implying that the model correctly classified 98% of the total instances in the testing dataset. This result indicates that the model is exceptionally effective in classifying instances into their respective pH levels with minimal misclassifications. For most of the classes, including pH 10, pH 4, pH 5, pH 6, pH 7, and pH 8, the precision, recall, and F1-score are 1.00, 1.00, and 1.00, respectively. These scores indicate that the model has correctly identified all instances of these pH classes in the testing dataset. However, for a few classes like pH 2, pH 3, pH

11, and pH 12, the precision, recall, and F1-score are less than 1.00, indicating that the model is not able to identify the instances of these classes 100% accurately. For instance, the explanation of the prediction results for the pH 2 and pH 3 classes is as follows. The pH 2 class exhibits a precision of 0.92, indicating that the model correctly predicted 92% of the instances as pH2. The recall is 1.00, implying that all actual pH 2 instances were correctly identified. The F1-score of 0.96 underscores the model's strong performance for pH 2. In the pH 3 class, the model achieved perfect precision but a recall of 0.92, indicating that it missed some actual pH 3 instances. The F1-score of 0.96 reflects the balanced performance of the model for pH 3.

Furthermore, **Figure 8** demonstrates the performance of the proposed model in terms of the confusion matrix. The obtained result indicates that for some classes, including pH 10, pH 4, pH 5, pH 6, pH 7, and pH 8, there are no misclassifications, and the proposed model is capable of classifying these images quite accurately. However, for a few classes like pH 12 and pH 3, the model is not able to correctly classify a few images. In the case of pH 12, there are three false negatives, indicating that the model missed three instances that were actually pH 12 and categorized them as pH 11. These are instances where the model failed to classify them as pH 12 correctly and made a Type II error. Similarly, the model has incorrectly recognized two instances from pH 2 and labeled them as pH 3. The test results show that the proposed deep learning-based classification model has great potential in classifying the images in their respective pH values and can be further explored for different applications.

3.5 Real meat sample spoilage detection

The freshness of real meat samples was determined before and after spoilage to examine the practical applicability of the microneedle-based colorimetric pH sensing patch for food quality monitoring applications. Figure 9a shows the optical image of a fresh meat sample that was obtained from the local supermarket. To understand the functionality of the integrated device using a realistic scenario, the pH values of the fresh and intentionally spoiled meat samples were detected using the developed pH-sensing patch, as shown in Figures 9b, 9c, and 9d. Figures 9b and 9d demonstrate the magnified images of the intentionally spoiled meat samples, whereas Figure 9c shows the magnified image of fresh meat samples considered for the experiments. It is important to note that the variations between the fresh and spoiled meat samples are challenging to capture via the naked eye, especially in mass food production and supply chain processes. To initialize the

experiment, the colorimetric pH sensing patches were placed on three different samples (as shown in Figure 9b, 9c, and 9d) and gently pushed so that the microneedle tips start extracting the fluid (a short video clip has been included in the supplementary file (Supplementary Video 3) to demonstrate the real-time fluid extraction from the meat sample). Once the fluid reached the absorption pad via the pH sensing strip, a smartphone was used to capture and crop the image of the patch for further machine learning-based analysis. As soon as a user uploads the cropped image and clicks on the predict button, the flask makes API calls and instructs the built-in model to run the computations in the back end. Next, the developed model predicts the pH value corresponding to the color of the uploaded image and displays both the uploaded image and pH value on the screen, as shown in Figures 9e, 9f, and 9g. It was noticed that the predicted pH values were in good agreement with the pH of the particular meat samples measured using a standard pH probe (PH700 Benchtop pH Meter Kit, Apera Instruments, LLC, Columbus, OH, USA). These findings allow us to determine that the developed machine learning-enabled pH sensing patch can be used as a colorimetric sensor for meat spoilage detection by older and color-blind individuals.

4. Conclusions

In this work, we have fabricated a low-cost, machine learning-enabled microneedle-based colorimetric pH sensing patch that can be utilized for both wound pH monitoring and meat spoilage detection. The device comprises a 3D printed microneedles array, hydrophilic membrane, sample pad, paper-based pH sensing strips, absorbent pad, and a transparent plastic membrane sandwiched between two adhesive patches. The structural, morphological, and mechanical characterization results confirmed that the microneedle array can be used for the fabrication of a pH-sensing patch for multipurpose applications. The skin penetration, autonomous fluid extraction, and transportation capability of the developed microneedle patch via surface tension were investigated using two skin-mimicking models, which confirmed the wound health monitoring potential of the sensing patch. Further, the pH detection performance of the machine learning model revealed that the proposed deep learning-based classification model has great potential in classifying the images in their respective pH values ranging from 2 to 12. Furthermore, the proof-of-concept study demonstrated that the developed pH sensing patch can easily be used as a colorimetric sensor for meat spoilage detection by older and color-blind persons using a smartphone.

Conflict of interest

There are no financial or personal conflicts to declare for the work reported in this paper.

Acknowledgments

The authors sincerely acknowledge the support received from the National Science Foundation (Award Number 2029974).

References

- [1] A. Pomberger, N. Jose, D. Walz, J. Meissner, C. Holze, M. Kopczynski, P. Müller-Bischof, A.A. Lapkin, Automated pH Adjustment Driven by Robotic Workflows and Active Machine Learning, Chemical Engineering Journal 451 (2023). https://doi.org/10.1016/j.cej.2022.139099.
- [2] Z. Li, W. Wan, Z. Bai, B. Peng, X. Wang, L. Cui, Z. Liu, K. Lin, J. Yang, J. Hao, F. Tian, Construction of pH-responsive nanoplatform from stable magnetic nanoparticles for targeted drug delivery and intracellular imaging, Sens Actuators B Chem 375 (2023). https://doi.org/10.1016/j.snb.2022.132869.
- [3] S. Mao, L. Zhang, J. Feng, P. Han, C. Lu, T. Zhang, Development of pH-responsive intelligent and active films based on pectin incorporating Schiff base (Phenylalanine/syringaldehyde) for monitoring and preservation of fruits, Food Chem 435 (2024). https://doi.org/10.1016/j.foodchem.2023.137626.
- [4] H. Tai, Q. Ding, D. Li, Y. Wei, Design of an intelligent PH sensor for aquaculture industry, in: IFIP Adv Inf Commun Technol, 2011. https://doi.org/10.1007/978-3-642-18369-0 77.
- [5] M.A.I. Shahrulakram, J. Johari, Water storage monitoring system with pH sensor for pharmaceutical plants, in: Proceedings of the 2016 6th International Conference on System Engineering and Technology, ICSET 2016, 2016. https://doi.org/10.1109/FIT.2016.7857536.
- [6] S. Kadian, G. Manik, N. Das, P. Roy, Targeted bioimaging and sensing of folate receptor-positive cancer cells using folic acid-conjugated sulfur-doped graphene quantum dots, Microchimica Acta 187 (2020). https://doi.org/10.1007/s00604-020-04448-8.
- [7] A. Kalkal, R. Pradhan, S. Kadian, G. Manik, G. Packirisamy, Biofunctionalized Graphene Quantum Dots Based Fluorescent Biosensor toward Efficient Detection of Small Cell Lung Cancer, ACS Appl Bio Mater 3 (2020). https://doi.org/10.1021/acsabm.0c00427.
- [8] S. Kadian, G. Manik, A highly sensitive and selective detection of picric acid using fluorescent sulfur-doped graphene quantum dots, Luminescence 35 (2020). https://doi.org/10.1002/bio.3782.
- [9] S. Shukla, J. Jakowski, S. Kadian, R.J. Narayan, Computational approaches to delivery of anticancer drugs with multidimensional nanomaterials, Comput Struct Biotechnol J 21 (2023) 4149–4158. https://doi.org/https://doi.org/10.1016/j.csbj.2023.08.010.
- [10] S.K. Sethi, S. Kadian, R. Gogoi, G. Manik, Layer-by-layer fabrication of self-cleaning superhydrophobic surface made from Carboxymethylcellulose and ZnO quantum dots: A combined experimental and computational study, Surfaces and Interfaces 37 (2023). https://doi.org/10.1016/j.surfin.2023.102752.
- [11] O. Eskilson, E. Zattarin, L. Berglund, K. Oksman, K. Hanna, J. Rakar, P. Sivlér, M. Skog, I. Rinklake, R. Shamasha, Z. Sotra, A. Starkenberg, M. Odén, E. Wiman, H. Khalaf, T. Bengtsson, J.P.E. Junker, R. Selegård, E.M. Björk, D. Aili, Nanocellulose composite wound dressings for real-time pH wound monitoring, Mater Today Bio 19 (2023). https://doi.org/10.1016/j.mtbio.2023.100574.
- [12] U. Heredia-Rivera, V. Kasi, A. Krishnakumar, S. Kadian, A.K. Barui, Z. He, H. Wang, L. Stanciu, R. Rahimi, Cold Atmospheric Plasma-Assisted Direct Deposition of Polypyrrole-Ag

- Nanocomposites for Flexible Electronic Sensors, ACS Appl Mater Interfaces 15 (2023) 17078–17090. https://doi.org/10.1021/acsami.2c20798.
- [13] U. Heredia-Rivera, S. Gopalakrishnan, S. Kadian, S. Nejati, V. Kasi, R. Rahimi, A wireless chipless printed sensor tag for real-time radiation sterilization monitoring, J Mater Chem C Mater (2022). https://doi.org/10.1039/d2tc00531j.
- [14] L.A. Schneider, A. Korber, S. Grabbe, J. Dissemond, Influence of pH on wound-healing: A new perspective for wound-therapy?, Arch Dermatol Res 298 (2007). https://doi.org/10.1007/s00403-006-0713-x.
- [15] A. Krishnakumar, S. Kadian, U. Heredia Rivera, S. Chittiboyina, S.A. Lelièvre, R. Rahimi, Organ-on-a-Chip Platform with an Integrated Screen-Printed Electrode Array for Real-Time Monitoring Trans-Epithelial Barrier and Bubble Formation, ACS Biomater Sci Eng (2022). https://doi.org/10.1021/acsbiomaterials.2c00494.
- [16] A. Krishnakumar, R.K. Mishra, S. Kadian, A. Zareei, U.H. Rivera, R. Rahimi, Printed graphene-based electrochemical sensor with integrated paper microfluidics for rapid lidocaine detection in blood, Anal Chim Acta 1229 (2022) 340332. https://doi.org/10.1016/J.ACA.2022.340332.
- [17] U. Heredia Rivera, S. Kadian, S. Nejati, J. White, S. Sedaghat, Z. Mutlu, R. Rahimi, Printed Low-Cost PEDOT:PSS/PVA Polymer Composite for Radiation Sterilization Monitoring, ACS Sens 7 (2022) 960–971. https://doi.org/10.1021/acssensors.1c02105.
- [18] S. Kadian, A. Kalkal, V. Jain, S. Shukla, R.J. Narayan, Pomegranate leaf extract-based carbon dots for the selective detection of 2,4,6-trinitrophenol, MRS Commun (2023). https://doi.org/10.1557/s43579-023-00430-6.
- [19] S. Kadian, G. Manik, A. Kalkal, M. Singh, R.P. Chauhan, Effect of sulfur doping on fluorescence and quantum yield of graphene quantum dots: An experimental and theoretical investigation, Nanotechnology 30 (2019). https://doi.org/10.1088/1361-6528/ab3566.
- [20] S.A. Machekposhti, S. Kadian, L. Vanderwal, S. Stafslien, R.J. Narayan, Novel hollow biodegradable microneedle for amphotericin B delivery, MedComm (Beijing) 4 (2023). https://doi.org/10.1002/mco2.321.
- [21] J.R. Sharpe, S. Booth, K. Jubin, N.R. Jordan, D.J. Lawrence-Watt, B.S. Dheansa, Progression of wound pH during the course of healing in burns, Journal of Burn Care and Research 34 (2013). https://doi.org/10.1097/BCR.0b013e31825d5569.
- [22] A. Krishnakumar, R.K. Mishra, S. Kadian, A. Zareei, U.H. Rivera, R. Rahimi, Printed graphene-based electrochemical sensor with integrated paper microfluidics for rapid lidocaine detection in blood, Anal Chim Acta 1229 (2022) 340332. https://doi.org/https://doi.org/10.1016/j.aca.2022.340332.
- [23] A. Zareei, V. Selvamani, S. Gopalakrishnan, S. Kadian, M.K. Maruthamuthu, Z. He, J. Nguyen, H. Wang, R. Rahimi, A Biodegradable Hybrid Micro/Nano Conductive Zinc Paste for Paper-Based Flexible Bioelectronics, Adv Mater Technol 7 (2022). https://doi.org/10.1002/admt.202101722.
- [24] V. Selvamani, S. Kadian, D.A. Detwiler, A. Zareei, I. Woodhouse, Z. Qi, S. Peana, A.M. Alcaraz, H. Wang, R. Rahimi, Laser-Assisted Nanotexturing and Silver Immobilization on Titanium Implant

- Surfaces to Enhance Bone Cell Mineralization and Antimicrobial Properties, Langmuir 38 (2022). https://doi.org/10.1021/acs.langmuir.2c00008.
- [25] S. Kadian, N. Chaulagain, H. Rajashekhar, D. Vrushabendrakumar, G. Manik, K. Shankar, An Ultrasensitive Fluorescent Paper Based Acidic Gas Sensing Platform, in: Proceedings of IEEE Sensors, 2021. https://doi.org/10.1109/SENSORS47087.2021.9639646.
- [26] S. Kadian, G. Manik, Sulfur doped graphene quantum dots as a potential sensitive fluorescent probe for the detection of quercetin, Food Chem 317 (2020). https://doi.org/10.1016/j.foodchem.2020.126457.
- [27] S.K. Sethi, S. Kadian, G. Manik, A Review of Recent Progress in Molecular Dynamics and Coarse-Grain Simulations Assisted Understanding of Wettability, Archives of Computational Methods in Engineering 29 (2022). https://doi.org/10.1007/s11831-021-09689-1.
- [28] S. Kadian, S. Shukla, R.J. Narayan, Probes for Noninvasive Biological Visualization and Biosensing of Cancer Cells, Appl Phys Rev 10 (2023). https://doi.org/https://doi.org/10.1063/5.0166740.
- [29] M. Singh, S. Kadian, G. Manik, Polymers in Adhesive Applications, in: Encyclopedia of Materials: Plastics and Polymers, 2022. https://doi.org/10.1016/B978-0-12-820352-1.00124-3.
- [30] O.A. Odeyemi, O.O. Alegbeleye, M. Strateva, D. Stratev, Understanding spoilage microbial community and spoilage mechanisms in foods of animal origin, Compr Rev Food Sci Food Saf 19 (2020). https://doi.org/10.1111/1541-4337.12526.
- [31] T.A. Tabish, Y. Zhu, S. Shukla, S. Kadian, G.S. Sangha, C.A. Lygate, R.J. Narayan, Graphene nanocomposites for real-time electrochemical sensing of nitric oxide in biological systems, Appl Phys Rev 10 (2023). https://doi.org/10.1063/5.0162640.
- [32] S. Kadian, N. Chaulagain, N.N. Joshi, K.M. Alam, K. Cui, K. Shankar, G. Manik, R.J. Narayan, Probe sonication-assisted rapid synthesis of highly fluorescent sulfur quantum dots, Nanotechnology 34 (2023) 30LT01. https://doi.org/10.1088/1361-6528/acd00a.
- [33] Z. Li, S. Kadian, R.K. Mishra, T. Huang, C. Zhou, S. Liu, Z. Wang, R. Narayan, Z. Zhu, Electrochemical detection of cholesterol in human biofluid using microneedle sensor, J Mater Chem B (2023). https://doi.org/10.1039/D2TB02142K.
- [34] V. Jackson, I.S. Blair, D.A. McDowell, J. Kennedy, D.J. Bolton, The incidence of significant foodborne pathogens in domestic refrigerators, Food Control 18 (2007). https://doi.org/10.1016/j.foodcont.2005.10.018.
- [35] S. Kadian, G. Manik, N. Das, P. Nehra, R.P. Chauhan, P. Roy, Synthesis, characterization and investigation of synergistic antibacterial activity and cell viability of silver-sulfur doped graphene quantum dot (Ag@S-GQDs) nanocomposites, J Mater Chem B 8 (2020). https://doi.org/10.1039/c9tb02823d.
- [36] A. Kalkal, S. Kadian, S. Kumar, G. Manik, P. Sen, S. Kumar, G. Packirisamy, Ti3C2-MXene decorated with nanostructured silver as a dual-energy acceptor for the fluorometric neuron specific enolase detection, Biosens Bioelectron 195 (2022). https://doi.org/10.1016/j.bios.2021.113620.
- [37] N. Chaulagain, K.M. Alam, S. Kadian, N. Kumar, J. Garcia, G. Manik, K. Shankar, Synergistic Enhancement of the Photoelectrochemical Performance of TiO2 Nanorod Arrays through Embedded

- Plasmon and Surface Carbon Nitride Co-sensitization, ACS Appl Mater Interfaces 14 (2022) 24309–24320. https://doi.org/10.1021/acsami.2c02649.
- [38] J. Xu, L. Guo, N. Zhao, X. Meng, J. Zhang, T. Wang, X. Wei, M. Fan, Response mechanisms to acid stress of acid-resistant bacteria and biotechnological applications in the food industry, Crit Rev Biotechnol 43 (2023). https://doi.org/10.1080/07388551.2021.2025335.
- [39] N. Husin, M.Z.A. Rahim, M.A.M. Noor, I.F.M. Rashedi, N. Hassan, Real-time monitoring of food freshness using delphinidin-based visual indicator, Malaysian Journal of Analytical Sciences 24 (2020).
- [40] S. Kadian, B.D. Arya, S. Kumar, S.N. Sharma, R.P. Chauhan, A. Srivastava, P. Chandra, S.P. Singh, Synthesis and Application of PHT-TiO2 Nanohybrid for Amperometric Glucose Detection in Human Saliva Sample, Electroanalysis 30 (2018). https://doi.org/10.1002/elan.201800207.
- [41] M. Chatterjee, P. Nath, S. Kadian, A. Kumar, V. Kumar, P. Roy, G. Manik, S. Satapathi, Highly sensitive and selective detection of dopamine with boron and sulfur co-doped graphene quantum dots, Sci Rep 12 (2022). https://doi.org/10.1038/s41598-022-13016-4.
- [42] S. Kadian, S.K. Sethi, G. Manik, Recent advancements in synthesis and property control of graphene quantum dots for biomedical and optoelectronic applications, Mater Chem Front 5 (2021). https://doi.org/10.1039/d0qm00550a.
- [43] S. Kadian, P. Kumari, S. Shukla, R. Narayan, Recent advancements in machine learning enabled portable and wearable biosensors, Talanta Open 8 (2023) 100267. https://doi.org/10.1016/J.TALO.2023.100267.
- [44] J.Y. Wang, L.J. Chen, X. Zhao, X.P. Yan, Silk fibroin-based colorimetric microneedle patch for rapid detection of spoilage in packaged salmon samples, Food Chem 406 (2023). https://doi.org/10.1016/j.foodchem.2022.135039.
- [45] Y. Wang, B. Gao, B. He, Toward Efficient Wound Management: Bioinspired Microfluidic and Microneedle Patch, Small 19 (2023). https://doi.org/10.1002/sml1.202206270.
- [46] Y. Shao, K. Dong, X. Lu, B. Gao, B. He, Bioinspired 3D-Printed MXene and Spidroin-Based Near-Infrared Light-Responsive Microneedle Scaffolds for Efficient Wound Management, ACS Appl Mater Interfaces (2022). https://doi.org/10.1021/acsami.2c16277.
- [47] S. Kadian, S.S. Sahoo, P. Kumari, R.J. Narayan, Machine learning enabled onsite electrochemical detection of lidocaine using a microneedle array integrated screen printed electrode, Electrochim Acta 475 (2024) 143664. https://doi.org/https://doi.org/10.1016/j.electacta.2023.143664.
- [48] S. Kadian, S. Gopalakrishnan, V. Selvamani, S. Khan, T. Meyer, R. Thomas, M.M. Rana, P.P. Irazoqui, M. Verma, R. Rahimi, Smart Capsule For Targeted Detection Of Inflammation Levels Inside The Gi Tract, IEEE Trans Biomed Eng (2023) 1–13. https://doi.org/10.1109/TBME.2023.3343337.
- [49] T. Kattenborn, J. Leitloff, F. Schiefer, S. Hinz, Review on Convolutional Neural Networks (CNN) in vegetation remote sensing, ISPRS Journal of Photogrammetry and Remote Sensing 173 (2021). https://doi.org/10.1016/j.isprsjprs.2020.12.010.

- [50] P. Kumari, D. Toshniwal, Long short term memory—convolutional neural network based deep hybrid approach for solar irradiance forecasting, Appl Energy 295 (2021). https://doi.org/10.1016/j.apenergy.2021.117061.
- [51] P. Kumari, D. Toshniwal, Impact of lockdown on air quality over major cities across the globe during COVID-19 pandemic, Urban Clim 34 (2020). https://doi.org/10.1016/j.uclim.2020.100719.
- [52] J. Watts, A. Potter, V. Mohan, P. Kumari, S.K. Thengane, S. Sokhansanj, Y. Cao, K.S. Kung, Proxy quality control of biomass particles using thermogravimetric analysis and Gaussian process regression models, Biofuels, Bioproducts and Biorefining (2023).
- [53] S. Praveen Chakravarthy, C. Gunasundari, K. Selva Bhuvaneswari, B. Sharma, S. Chowdhury, Convolutional Neural Network (CNN) for Image Detection and Recognition in Medical Diagnosis, in: IET Conference Proceedings, 2022. https://doi.org/10.1049/icp.2023.0579.
- [54] P. Kumari, D. Toshniwal, Real-time estimation of COVID-19 cases using machine learning and mathematical models-The case of India, in: 2020 IEEE 15th International Conference on Industrial and Information Systems, ICIIS 2020 Proceedings, 2020. https://doi.org/10.1109/ICIIS51140.2020.9342735.
- [55] P. Kumari, D. Toshniwal, Deep learning models for solar irradiance forecasting: A comprehensive review, J Clean Prod 318 (2021). https://doi.org/10.1016/j.jclepro.2021.128566.
- [56] S. Cong, Y. Zhou, A review of convolutional neural network architectures and their optimizations, Artif Intell Rev 56 (2023). https://doi.org/10.1007/s10462-022-10213-5.
- [57] P. Kumari, D. Toshniwal, Impact of lockdown measures during COVID-19 on air quality—A case study of India, Int J Environ Health Res 32 (2022). https://doi.org/10.1080/09603123.2020.1778646.
- [58] P. Kumari, D. Toshniwal, Advanced machine learning techniques for short-term solar irradiance forecasting, in: Proceedings of the International Conference on AI-ML Systems (AI-ML Systems' 21). ACM, 2021: p. 4.
- [59] P. Kumari, D. Toshniwal, Machine learning techniques for hourly global horizontal irradiance prediction: A case study for smart cities of India, in: International Conference on Applied Energy (ICAE), 2021: pp. 1–6.
- [60] P. Kumari, D. Toshniwal, Extreme gradient boosting and deep neural network based ensemble learning approach to forecast hourly solar irradiance, J Clean Prod 279 (2021). https://doi.org/10.1016/j.jclepro.2020.123285.
- [61] P. Kumari, R. Wadhvani, Wind Power Prediction Using KLMS Algorithm, in: Proceedings of the International Conference on Inventive Research in Computing Applications, ICIRCA 2018, 2018. https://doi.org/10.1109/ICIRCA.2018.8597419.
- [62] M. Makarkin, D. Bratashov, State-of-the-art approaches for image deconvolution problems, including modern deep learning architectures, Micromachines (Basel) 12 (2021). https://doi.org/10.3390/mi12121558.

- [63] G.A. Vargas-Hákim, E. Mezura-Montes, H.G. Acosta-Mesa, A Review on Convolutional Neural Network Encodings for Neuroevolution, IEEE Transactions on Evolutionary Computation 26 (2022). https://doi.org/10.1109/TEVC.2021.3088631.
- [64] S. Mascarenhas, M. Agarwal, A comparison between VGG16, VGG19 and ResNet50 architecture frameworks for Image Classification, in: Proceedings of IEEE International Conference on Disruptive Technologies for Multi-Disciplinary Research and Applications, CENTCON 2021, 2021. https://doi.org/10.1109/CENTCON52345.2021.9687944.
- [65] P. Kumari, D. Toshniwal, HOURLY SOLAR IRRADIANCE PREDICTION FROM SATELLITE DATA USING LSTM, 2019.
- [66] P. Kumari, D. Toshniwal, Analysis of ANN-based daily global horizontal irradiance prediction models with different meteorological parameters: a case study of mountainous region of India, Int J Green Energy 18 (2021). https://doi.org/10.1080/15435075.2021.1890085.
- [67] Z. Faraji Rad, P.D. Prewett, G.J. Davies, Rapid prototyping and customizable microneedle design: Ultra-sharp microneedle fabrication using two-photon polymerization and low-cost micromolding techniques, Manuf Lett 30 (2021). https://doi.org/10.1016/j.mfglet.2021.10.007.
- [68] V. Ebrahiminejad, P.D. Prewett, G.J. Davies, Z. Faraji Rad, Microneedle Arrays for Drug Delivery and Diagnostics: Toward an Optimized Design, Reliable Insertion, and Penetration, Adv Mater Interfaces 9 (2022). https://doi.org/10.1002/admi.202101856.
- [69] S. Shukla, S.A. Machekposhti, N. Joshi, P. Joshi, R.J. Narayan, Microneedle-Integrated Device for Transdermal Sampling and Analyses of Targeted Biomarkers, Small Science (2023). https://doi.org/10.1002/smsc.202200087.

List of Figures

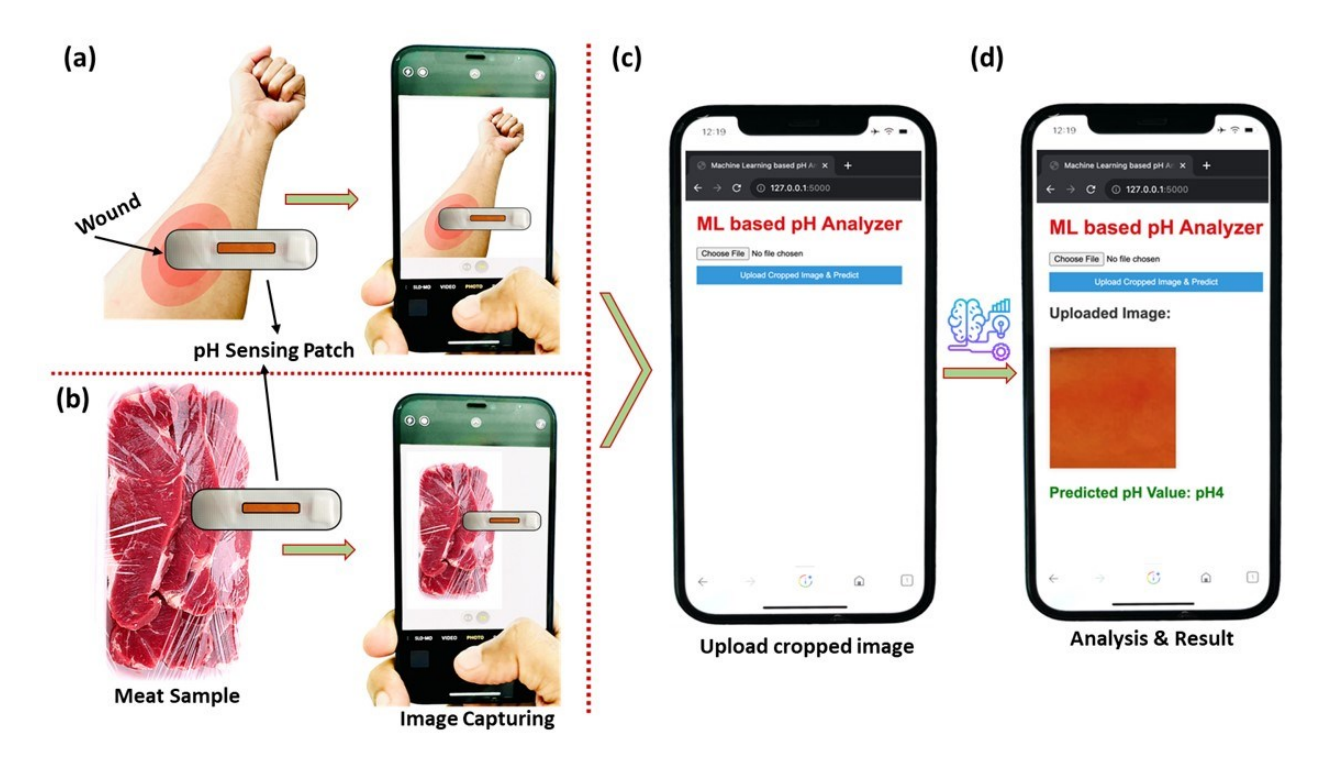


Figure 1: Schematic diagram of machine learning-enabled microneedle-based colorimetric pH sensing patch for wound health monitoring and packaged meat spoilage detection application. (a) Capturing the photo of the pH sensing patch applied on the wound present at the forearm for wound health monitoring, (b) Capturing the photo of the pH sensing patch applied on packaged meat for spoilage detection, (c) Upload the cropped image of the pH sensing strip and (d) Analysis of the pH value using the developed machine learning model.

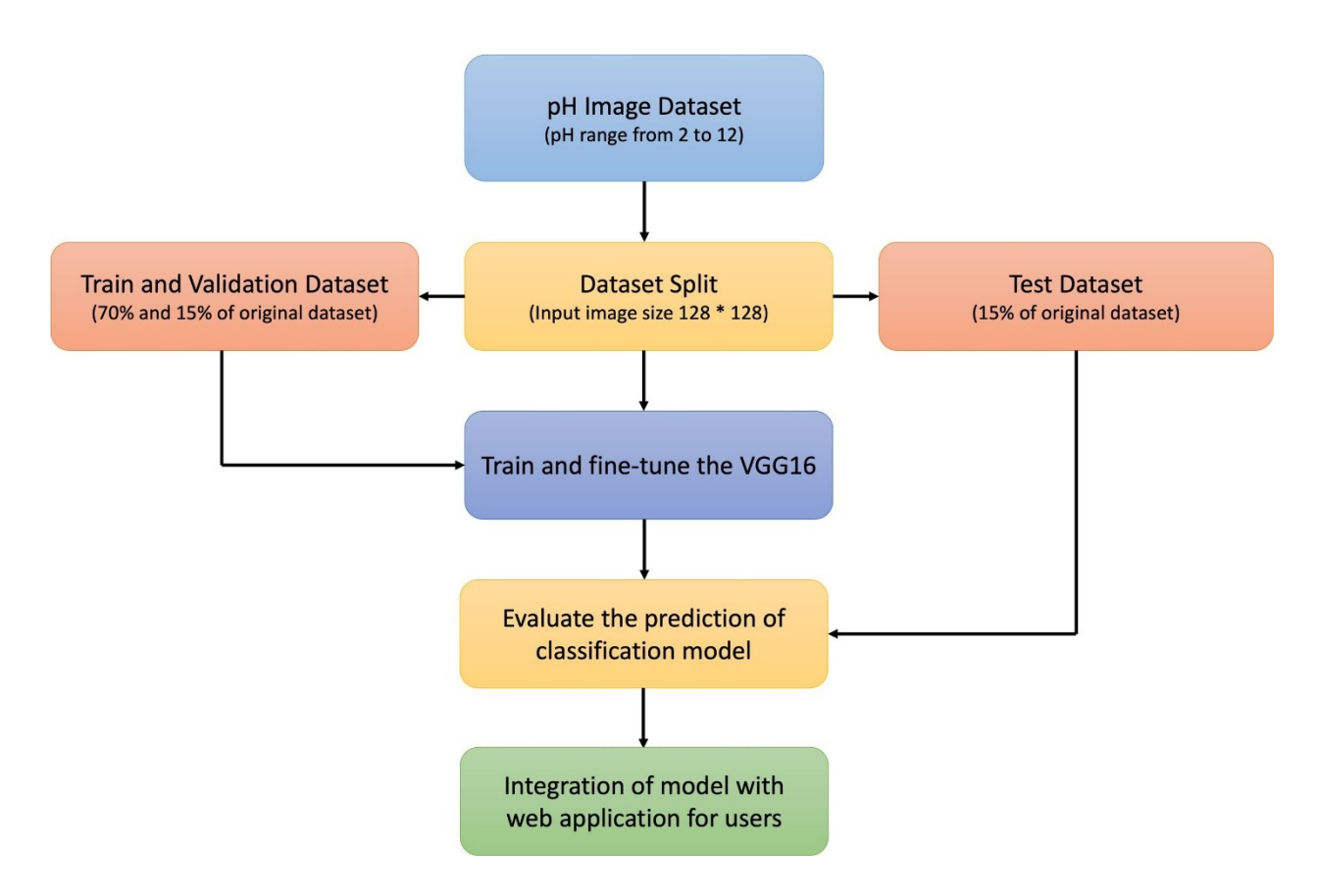


Figure 2: Demonstration of simplified flow chart of machine learning-based image classification model used in this study.

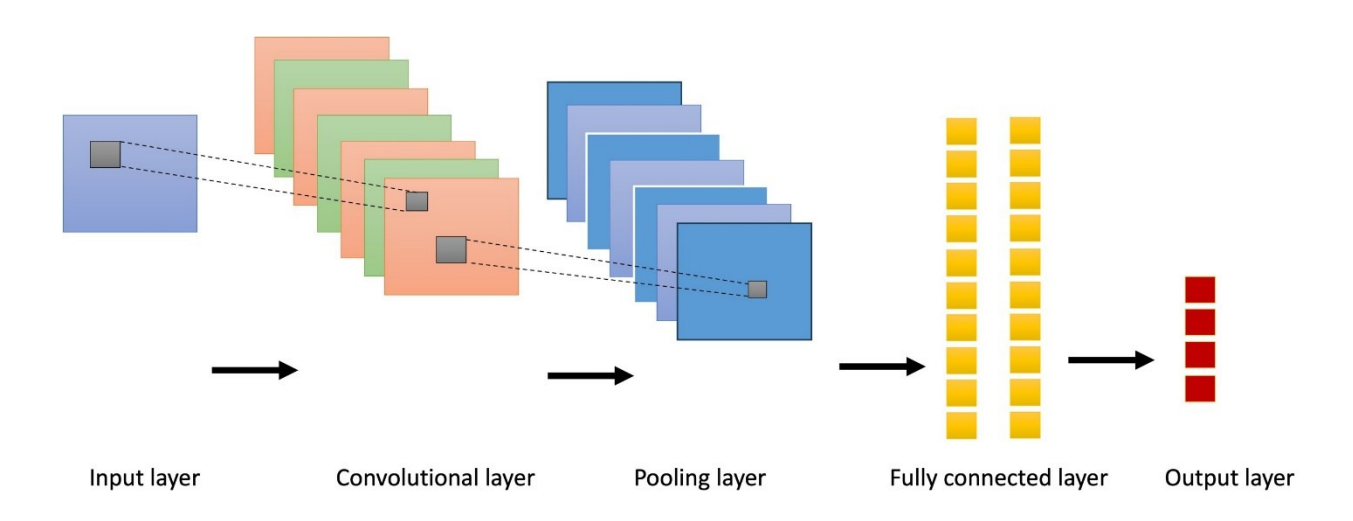


Figure 3: Illustration of the design and basic architecture of a CNN model used in this study.

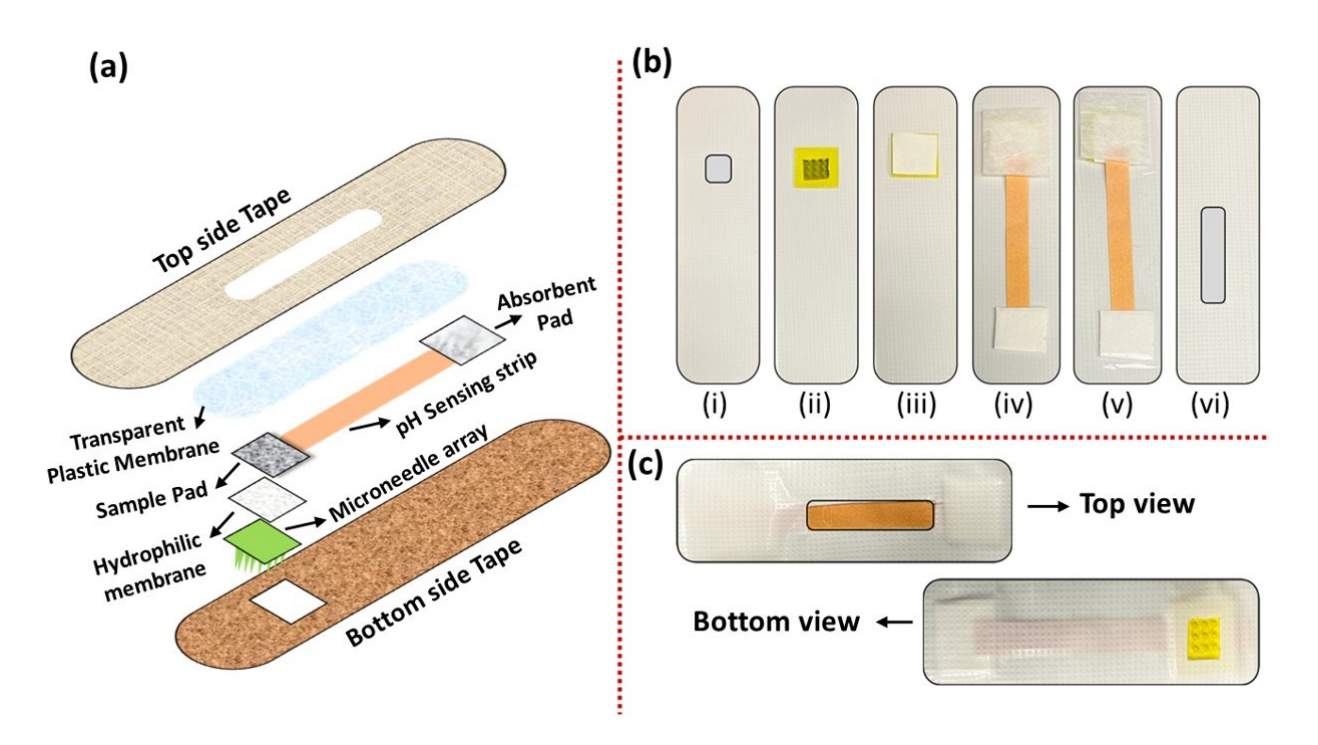


Figure 4: Illustration of the manufacturing process for the microneedle-based colorimetric pH sensing patch. (a) View of different components used in the manufacturing of pH sensing patch, (b) real-time images of the stepwise (i-vi) fabrication process of the microneedle array-based pH sensing patch, and (c) top and bottom view of the fully assembled pH sensing patch.

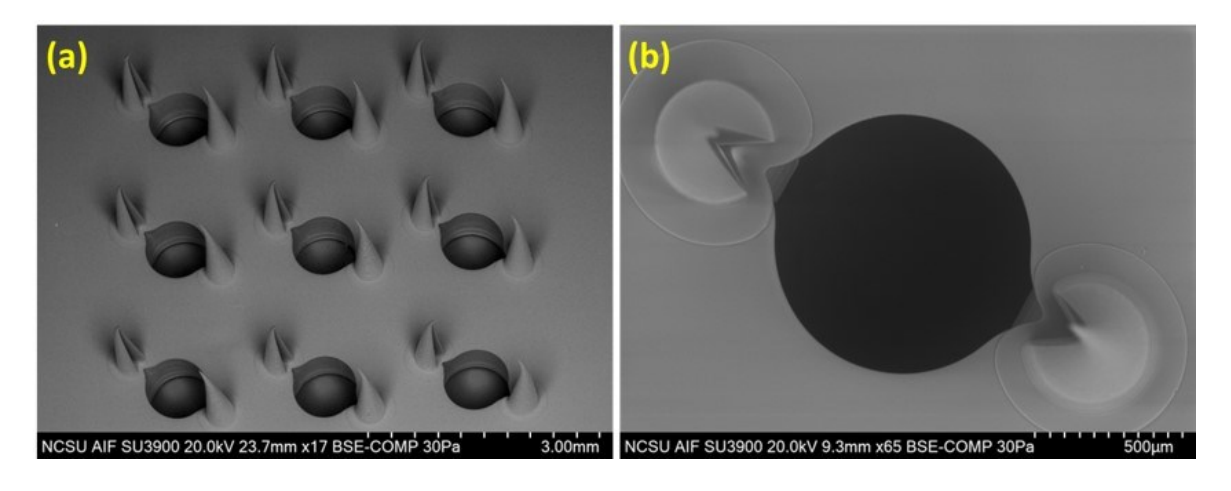


Figure 5: Illustration of (a) SEM images of the 3D printed microneedle array and (b) magnified SEM image of microneedle array containing open side channels and a reservoir at the base.

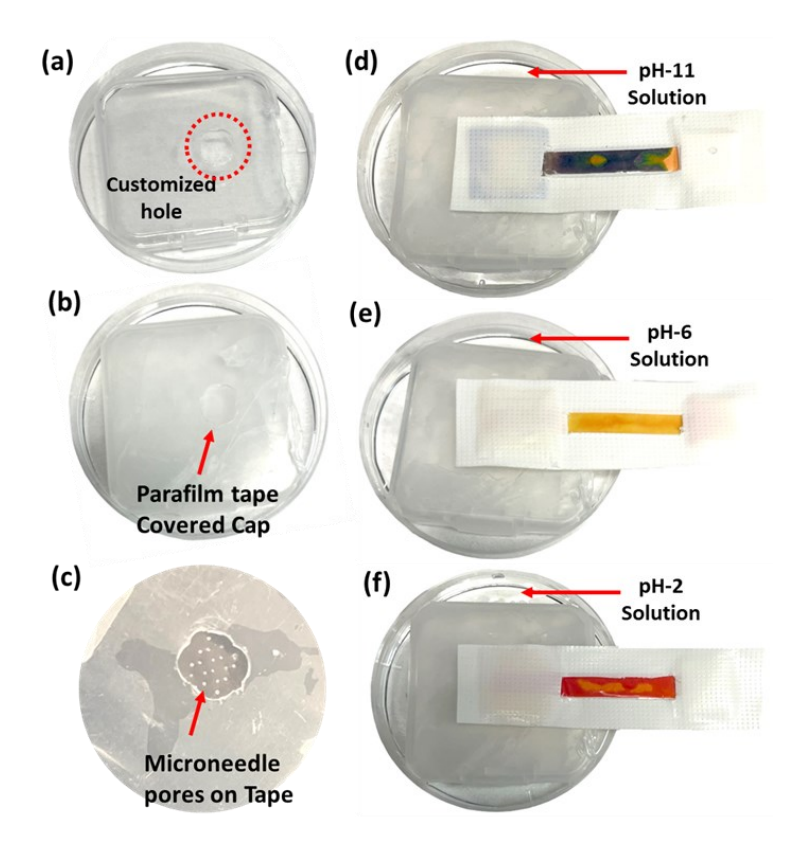


Figure 6: Proof-of-concept demonstration of the integrated device by showing the pH sensing capability through skin-mimicking parafilm tape. (a) Illustration of an 8 mm diameter customized hole created in the cap of a small plastic box and placed in a small Petri dish, (b) circular hole covered with skin mimicking parafilm tape, (c) Illustration of the optical image of pores created by the microneedle array on the parafilm tape after experiments, and (d-f) Petri dish filled with different pH (11, 6 and 2) solutions, respectively.

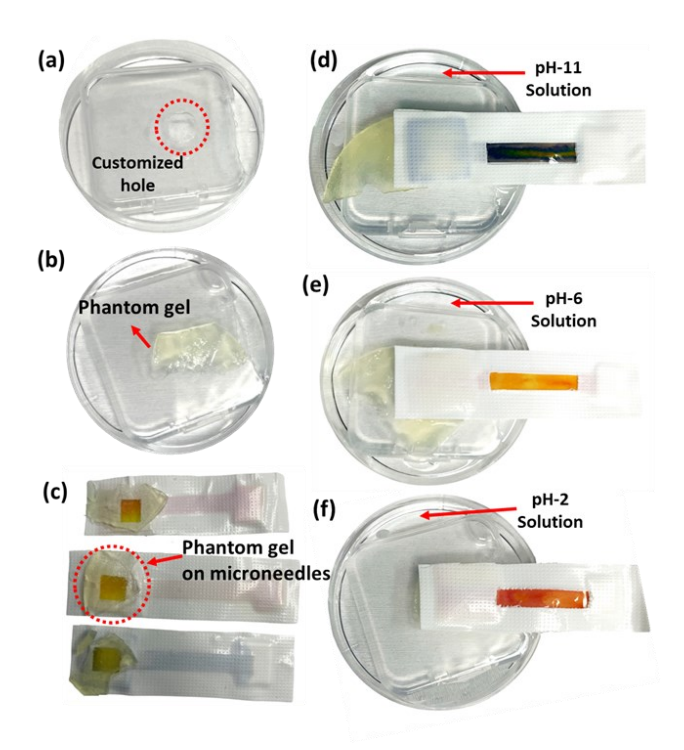


Figure 7: Proof-of-concept demonstration of the fully assembled device by showing the pH sensing capability through skin-mimicking phantom gel. (a) Illustration of an 8 mm diameter customized hole created in the cap of a small plastic box and placed in a small Petri dish, (b) circular hole covered with skin mimicking phantom gel, (c) illustration of the optical image of phantom gel attached on the microneedle array after experiments, and (d-f) Petri dish filled with different pH (11, 6, and 2) solutions, respectively.

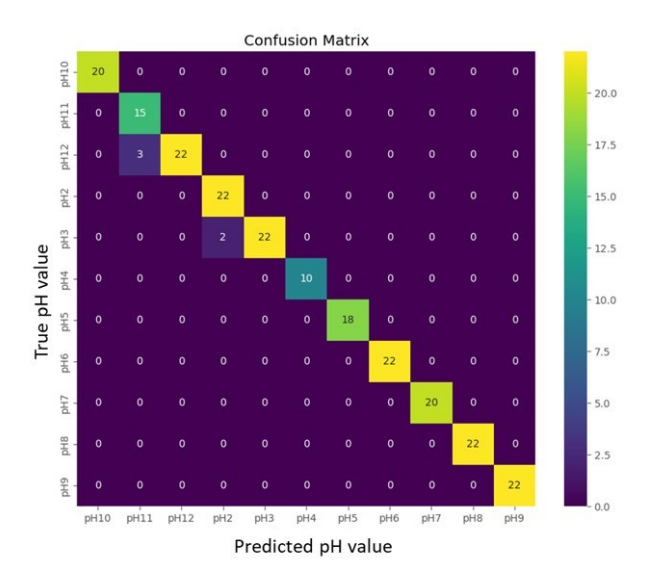


Figure 8: Illustration of confusion matrix for pH value classification.

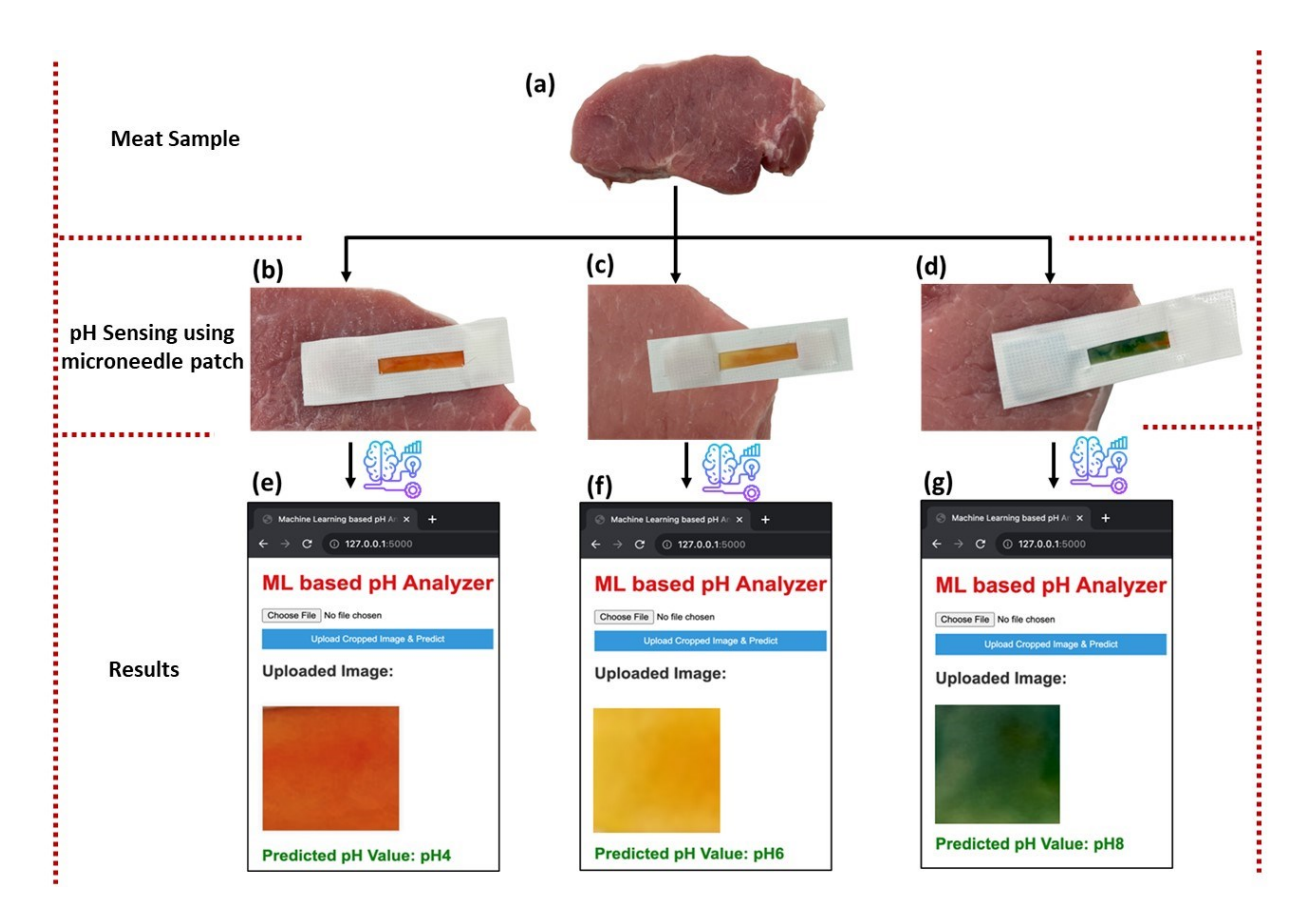


Figure 9: Proof-of-concept demonstration and real meat spoilage detection using microneedle-based pH sensing patch and digital visualization through the machine learning-based web application. Optical image of (a) the real meat sample, (b) the intentionally spoiled meat sample by exposing it to an acidic solution, (c) the fresh meat sample, (d) the intentionally spoiled meat sample by exposing it to a basic solution and (e-f) Screenshots of the developed web application demonstrating the prediction of pH value for real meat sample.

List of Tables

Table 1. Classification report of the developed classification model for testing dataset.

	Precision	recall	F1-score	support
pH2	0.92	1.00	0.96	22
рН3	1.00	0.92	0.96	24
pH4	1.00	1.00	1.00	10
pH5	1.00	1.00	1.00	18
рН6	1.00	1.00	1.00	22
pH7	1.00	1.00	1.00	20
рН8	1.00	1.00	1.00	22
pH9	1.00	1.00	1.00	22
pH10	1.00	1.00	1.00	20
pH11	0.83	1.00	0.91	15
pH12	1.00	0.88	0.94	25
accuracy			0.98	220